Propulsion and Power Research 2020;xxx(xxx):1−19

http://ppr.buaa.edu.cn/

Propulsion and Power Research

www.sciencedirect.com

ORGINAL ARTICLE

Dense core response to forced acoustic fields in oxygen-hydrogen rocket flames

Youhi Morii[a,b,*], Scott Beinke[c], Justin Hardi[c], Taro Shimizu[a], Hideto Kawashima[d], Michael Oschwald[c,e]

[a]*Research and Development Directorate, JAXA, Sagamihara, 252-5210, Japan*
[b]*Institute of Fluid Science, Tohoku University, Sendai, 980-8577, Japan*
[c]*Institute of Space Propulsion, DLR, Lampoldshausen, 74239, Germany*
[d]*Research and Development Directorate, JAXA, Tsukuba, 305-0047, Japan*
[e]*Institute of Jet Propulsion and Turbomachinery, RWTH, Aachen, 52062, Germany*

Received 24 April 2019; accepted 16 June 2020
Available online XXXX

KEYWORDS

Liquid rocket engine;
Combustion instability;
Computational fluid dynamics (CFD);
Large eddy simulation (LES);
Supercritical fluid

Abstract Oscillatory combustion representative of thermo-acoustic instability in liquid rockets is simulated by experiment and LES calculation to investigate the flame behavior in detail. In particular, we focus on how the velocity and pressure fluctuations affect the behavior of the dense oxygen jet, or 'LOx core'. The test case investigated is a high pressure, multi-injector, oxygen-hydrogen combustor with a siren for acoustic excitation. First, the LES calculation is validated by the resonant frequencies and average flame topology. A precise frequency correction is conducted to compare experiment with LES. Then an unforced case, a pressure fluctuation case, and a velocity fluctuation case are investigated. LES can quantitatively reproduce the LOx core shortening and flattening that occurs under transverse velocity excitation as it is observed in the experiments. On the other hand, the core behavior under pressure excitation is almost equal to the unforced case, and little shortening of the core occurs. The LOx core flattening is explained by the pressure drop around an elliptical cylinder using the unsteady

*Corresponding author.
E-mail address: morii@edyn.ifs.tohoku.ac.jp (Youhi Morii).
Peer review under responsibility of Beihang University.

Production and Hosting by Elsevier on behalf of KeAi

https://doi.org/10.1016/j.jppr.2020.06.001

Bernoulli equation. Finally, it is shown that the shortening of the LOx core occurs because the flattening enhances combustion by mixing and increase of the flame surface area.

1. Introduction

In the development of rockets powered by liquid propellants, the engine is the most challenging and critical component. Combustion instability is a problem which can greatly complicate engine development. Inside the combustion chamber of a liquid rocket engine, turbulent diffusion flames are formed between the fuel and oxidizer flows, so high levels of combustion noise are generated. However, if the amplitude of the noise exceeds more than a few percents of the mean chamber pressure the consequences for the engine can be disastrous. Oscillatory combustion coupled with acoustic modes, usually called high-frequency (HF) instability, can cause the noise to reach dangerously high amplitudes and is still an unresolved problem [1]. Tangential modes are historically the most destructive as a corresponding increase in the heat transfer rate can melt the chamber walls [2].

In recent years, experiments in oxygen-hydrogen (LOx/H_2) and oxygen-methane (LOx/CH_4) rocket combustors with optical access using siren excitation have been carried out to investigate the flame response under conditions simulating combustion instability [3–9]. It has been reported from visualizations how the flame responds to acoustic perturbations; for example how the length and shape of the intact part of the dense oxygen jet, or 'LOx core', are greatly affected by a transverse acoustic field [10]. However, it is difficult to obtain detailed, quantitative information experimentally. Therefore numerical modeling is being employed to investigate combustion instability phenomena in detail.

A recent example of the use of CFD to study this problem is from Hakim et al. [11,12], who reproduced experiments performed with LOx/CH_4. They reported that the LOx core length is shortened under tangential mode excitation, and that the core is flattened. In addition, they described how the LOx core shape can be explained by the pressure drop at the edge of the core using Bernoulli's theory. The effects of Strouhal number and velocity fluctuation on the core are also explained by Gonzalez-Flesca et al. [13] using numerical simulations of a supercritical nitrogen jet.

While these works discuss the effect of transverse acoustic velocity in detail, numerical simulations have not been performed for the case of LOx/H_2 combustion under transverse acoustic perturbation. Furthermore, the effect of acoustic pressure fluctuation on the flame is not discussed to such depth in the previous studies. Our objective is, therefore, to investigate whether pressure or velocity fluctuations have a greater effect on LOx/H_2 rocket flames using large eddy simulations (LES) to better understand LOx/H_2 combustion instabilities.

In this work, an experimental LOx/H_2 rocket combustor with siren excitation is modeled numerically with the LES approach. Work on this test case began in the frame of the 3rd Modeling Workshop of the Rocket Engine Stability iniTiative (REST), a cooperation of French and German industrial and institutional partners. In this paper, the LES results are first compared with the experimental resonant frequency and amplitude with and without siren excitation. Then the flame topology as defined by the LOx cores is compared with the experimental visualization results. These aspects serve to build confidence in the ability of the model to recreate the experimental conditions. After demonstrating a sufficient match between LES and experiments, the dynamic LOx core response to transverse acoustic velocity and acoustic pressure are investigated. The LES simulations are also extended to pressure amplitudes beyond those achieved in the experiment. It will be shown how the LOx core length and form responds significantly under transverse acoustic forcing, but insignificantly under pressure forcing. Bernoulli's theory is also extended to an elliptical geometry more representative of the deformed core.

2. Experimental test case

The test case modeled in this work was provided by the Rocket Propulsion Department at the DLR Institute of Space Propulsion, near Lampoldshausen, Germany. The experiment is named combustor 'H', abbreviated 'BKH', and was developed to investigate the interaction of LOx/H_2 combustion and acoustics under conditions relevant for industrial engines [14]. BKH is operated at the European Research and Technology Test Facility P8 for cryogenic rocket engines, also at the DLR Lampoldshausen site. The combustor design was inspired by two other experiments; the Common Research Combustor (CRC) [5], and the Multi Injector Combustor (MIC) [15]. As illustrated in Figure 1, the combustion chamber of BKH has a rectangular cross section and a siren excitation system for acoustically forcing the chamber at frequencies typical of real instabilities. Optical access to the near-injector region is provided through windows in both sides of the chamber. High speed visualization techniques have been applied to spatially and temporally resolve the

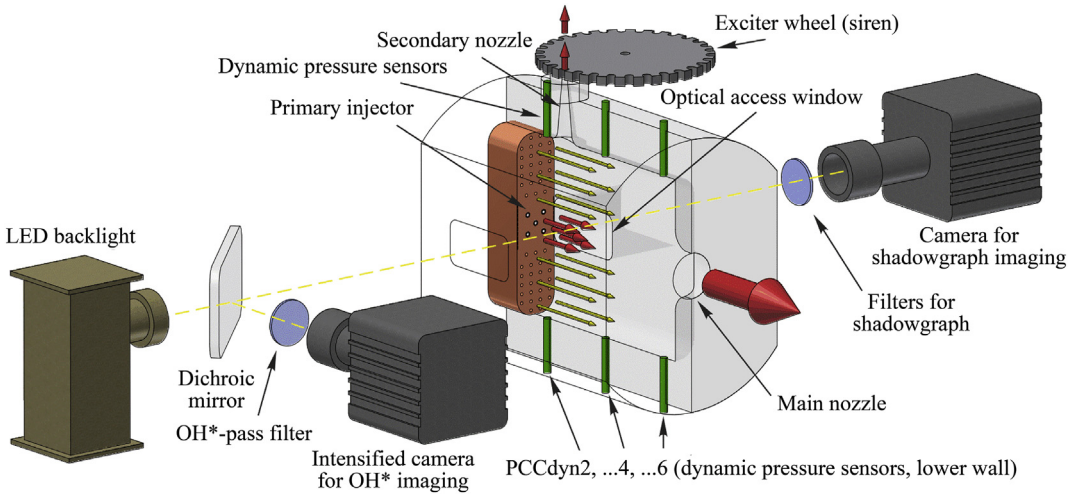

Figure 1 Illustration of combustor 'H' (BKH) and the optical setup.

response of the LOx spray and flame to the forced acoustic excitation.

2.1. Injection system

The propellants are injected axially through the injector at the front of the chamber. There are five shear-coaxial, 'primary' injection elements which are representative of upper stage engines in dimension, flow rate, and layout pattern. The five elements are arranged in a 'matrix' pattern, with one central, and four equally spaced injectors surrounding it. A film of ambient temperature H_2 is injected from linear slots at the walls either side of the primary injection elements to protect the optical windows from high temperatures in the reaction zone. A further co-flow of secondary H_2 is injected from a total of 50 simple orifices arranged in arrays in the faceplate above and below the primary injection elements. This 'secondary' H_2 serves to lower the ratio of oxidizer to fuel mass flow rate (ROF) of the bulk equilibrium mixture in the chamber and thereby minimize the thermal loads on the combustor and siren system. It also provides a more uniform acoustic environment and reduces the recirculation of combustion products at the faceplate. The chamber has been operated at pressures up to 8 MPa, which is supercritical for oxygen. In this work a single operating condition is considered, namely 6 MPa chamber pressure with a ROF of 6 in the five primary injection elements.

2.2. Acoustic excitation

There is an axial main nozzle at the end of the BKH chamber, and a secondary nozzle located in the upper wall of the chamber a short distance downstream of the injection plane, oriented perpendicularly to the direction of main flow in the chamber. The exciter wheel of the siren periodically blocks the exhaust flow through this nozzle to produce pressure fluctuations which propagate back down into the combustion chamber and excite the acoustic resonance modes of the volume. Usually, the excitation frequency is linearly increased over the course of a test firing in order to pass through and excite two or more acoustic modes in a single test.

An example test profile is shown in Figure 2. At around 18 s the excitation frequency passes through and excites the first longitudinal (1L) mode of the combustion chamber, and at around 32 s the first transverse (1T) mode is excited. Excitation of either the 1L or 1T mode can be used to separately study the influence on the flame of acoustic pressure or transverse acoustic velocity, respectively. Flush-mounted dynamic pressure sensors for acoustic measurements, indicated in Figure 1, as well as conventional sensors for temperature and pressure measurements, are located throughout the combustion chamber and injector.

2.3. Operating condition and cases

Three test cases are addressed in this work, obtained from three separate test runs. They are defined by the acoustic excitation condition at the time of an appropriate

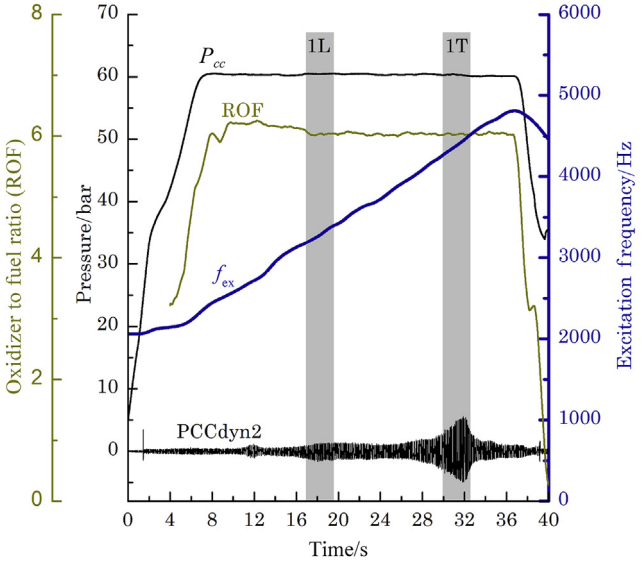

Figure 2 Example test sequence of BKH with ramped acoustic excitation.

sample of shadowgraph imaging. The first case is an unexcited condition, from a test where the siren was not in operation and the secondary nozzle was open to atmosphere. Data defining the second and third cases are from test runs using the sequence depicted in Figure 2. The second case is during forced excitation of the 1L mode, corresponding to the conditions around 18 s in Figure 2. The third case is from the very test run depicted in Figure 2 at 31.2 s, during excitation of the 1T mode.

2.4. Optical diagnostics

During excitation of the 1L or 1T mode, high-speed cameras are triggered to record the response of the flame via the optical access windows. Backlit shadowgraph imaging for observation of the dense oxygen jets and filtered OH^* radiation for the reaction zone are operated in parallel. A simplified schematic illustration of the optical setup can be seen in Figure 1. In this work, experimental observations based on shadowgraph imaging will be considered. Example shadowgraph images from the 6 MPa, ROF 6 operating condition for three different acoustic conditions are shown in Figure 3. The upper row shows instantaneous images and the lower row time-averaged images. The images on the left side are from the unexcited case, without acoustic forcing, in the center are images from the 1L case, and on the right side are images taken from time 31.1−31.2 s in the test in Figure 2, where the 1T mode is excited to 0.81 MPa amplitude, peak to peak.

3. Numerical model

3.1. Numerical method

The governing equations are three-dimensional filtered compressible Navier-Stokes equations, which include the conservation equations of mass, momentum, energy, and mixture fraction. In this study, an unstructured solver FaSTAR (FaST Aerodynamic Routines) [16] developed at the JAXA Institute of Aeronautical Technology is adopted. The LES approach is used with the Wall-Adapting Local Eddy-viscosity (WALE) model [17]. The advection fluxes are evaluated by the SLAU2 scheme [18], and the viscous and diffusion terms are computed by the central differential formulae with the tighter-coupling correction. The time integration is carried out by a LU-SGS implicit method with three internal iterations. The time step size was limited by CFL conditions, and the maximum CFL number was set around 2 to reproduce the unsteady phenomena accurately.

In the simulation, one phase fluid is assumed because it is well-known that the flow under supercritical conditions could be treated as a dense gas. For very high density fluid properties, Soave-Redlich-Kwong (SRK) equation of state (EOS) is adopted for the state equation and thermodynamic properties. The viscosity and thermal conductivity are modified by the method of Chung et al. [19]. The critical constants are taken from Ref. [20,21]. In this study, we adopt the laminar flamelet concept and alter the chemical reaction calculations by look-up table constructed by detailed one-dimensional counter-flow H_2/O_2 diffusion flame simulations. The 8 species (H_2, O_2, OH, H_2O, H, O, H_2O_2, HO_2) and 21 elementary reaction model proposed by Li et al. [22] is employed to model the H_2/O_2 reaction system at high pressures. The chemistry table used in this study provides the mass fractions of components with the inputs of mixture fraction, scalar dissipation rate, and fluctuation of mixture fraction. The mixture fraction is defined by the method of Bilger [23] and the stoichiometric mixture fraction is 0.111.

3.2. Numerical conditions

The mesh system is mainly composed with hexahedra mesh (See Figure 4). The minimum cell width is 66 μm and the total mesh consists of 9.3 M cells. The grid convergence was investigated under the excited 1T mode condition which is the condition that the LOx core length was characteristically changed. The results of the LOx core length using the coarse mesh (1.3 M cells) agreed well with the results using the fine mesh (9.3 M cells). In this paper, results with the fine mesh shown in Figure 4 are presented.

Next, the numerical boundary conditions are described. Figure 5 shows the summary of the boundaries, and Tables 1−3 show the boundary conditions and total mass flow rate values. In the experiments, the respective injectors are fed by injection manifolds. Therefore, primary H_2 and LOx should

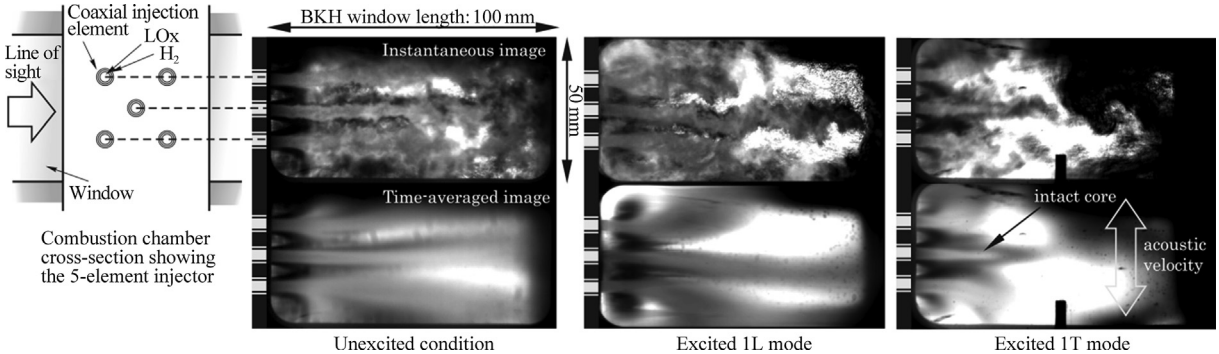

Figure 3 Example shadowgraph imaging from the experiment. From left to right: unexcited, excited 1L mode, excited 1T mode. Upper row: instantaneous images. Lower row: time-averaged images.

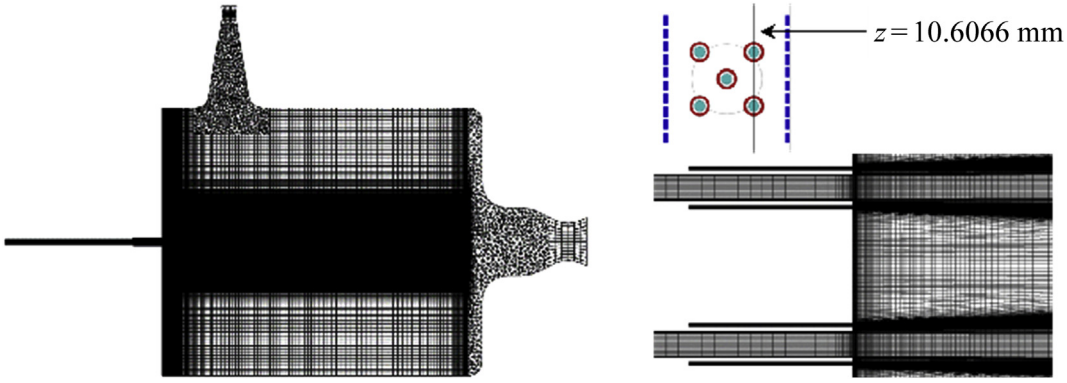

Figure 4 Mesh system of *xy* plane at $z = 0.0$ mm (upper) and the zoom at $z = 10.61$ mm.

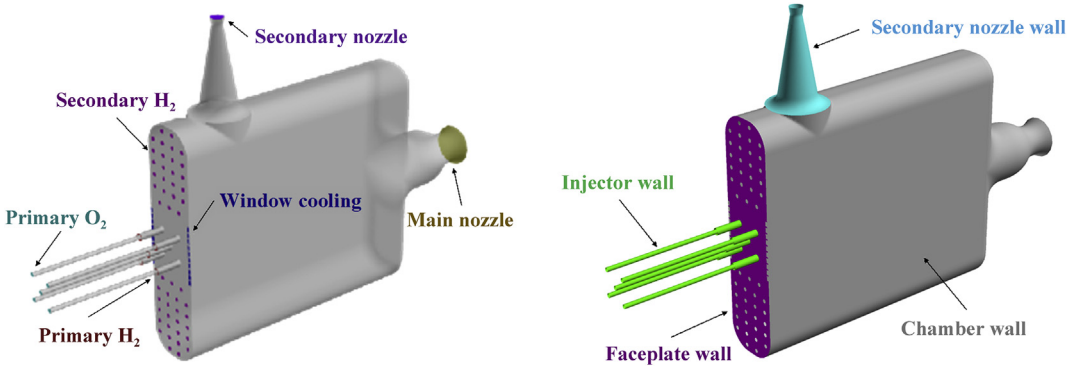

Figure 5 Summary of boundaries for LES simulations.

be divided by 5 for per-element values, Secondary H_2 by 50, and window cooling H_2 by 20. The lengths of the injectors were determined by making the inlet correspond to the position of pressure nodes of their longitudinal (organ pipe) acoustic modes to obtain the realistic boundary conditions.

Table 1 Summary of injector boundary conditions.

	Temperature/K	Mass flow rate/($\times 10^{-3}$ kg/s)
Primary H_2	279	95 (5 injectors)
Primary O_2	127	565 (5 injectors)
Secondary H_2	278	899 (50 injectors)
Window cooling H_2	281	260 (20 injectors)

Table 2 Summary of wall boundary conditions.

	Boundary condition
Chamber wall	Slip wall, adiabatic
Injector wall	Non-slip wall, adiabatic
Faceplate wall	Non-slip wall, adiabatic
Secondary nozzle wall	Non-slip wall, adiabatic

Table 3 Summary of outlet boundary conditions.

	Unexcited cases	Excited cases
Main nozzle	0^{th} order extrapolation	0^{th} order extrapolation
Secondary nozzle	0^{th} order extrapolation	Slip wall/0.1 MPa pressure

The boundary conditions indicated in Tables 1−3 were the same for all acoustic cases. All walls are assumed to be adiabatic. The boundary conditions of injectors and faceplate walls are non-slip wall and others are slip wall. The outlet conditions of the main and secondary nozzles are zero-order extrapolation for the case without siren excitation. With siren excitation, the outlet condition of the secondary nozzle is switched alternately from a 0.1-MPa pressure boundary to a slip wall boundary condition at the 1L or 1T frequency.

4. Results and discussion

4.1. Comparison of the resonant modes

4.1.1. CFD result of unexcited case

First, the calculation of the unexcited case was carried out without forcing for about 100 ms until the result stabilized. After that, to implement the FFT analysis, the calculation was performed for a further 60 ms.

The pressure history at PCCdyn2 and its PSD are shown in Figure 6. Note that the peak in the experimental data below 3 kHz is an artifact, and that the PSD is normalized by the chamber pressure to compare the CFD results with the experimental data in Figure 6. The time average combustion chamber pressure (P_{cc}) is 5.88 MPa, which is in good agreement with measure pressure of 6.07 MPa in the experiment.

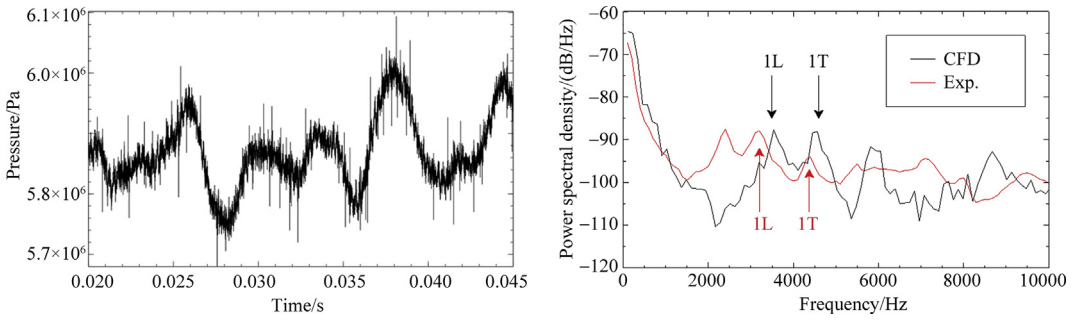

Figure 6 Pressure history (left) and PSD (right) at the location of PCCdyn2.

From the PSD, the frequencies of the 1L and 1T modes in the numerical simulation are identified as 3491 and 4595 Hz, respectively. These values are higher than those obtained in the experiment which were 3395 Hz (1L) and 4373 Hz (1T). A description of these differences is provided in a later section. The acoustic amplitude of PCCdyn2 is calculated from the bandpass filtered power spectral density. The bandpass filtered amplitudes are 2862 Pa between 3441 and 3541 Hz for the 1L mode and 2197 Pa between 4545 and 4645 Hz for the 1T mode. The bandpass filtered amplitude in experiments are 1900 Pa between 3345 and 3445 Hz for the 1L mode and 1544 Pa between 4323 and 4423 Hz for the 1T mode. Comparing with the experimental data, the numerical amplitudes are around 51% higher for the 1L and 42% higher for the 1T modes.

From these results, the frequencies to be used for siren excitation in the subsequent 1L and 1T mode numerical cases are determined to be 3491 Hz and 4595 Hz, respectively.

4.1.2. CFD results of acoustically forced cases

Using the quasi-steady unexcited case result at 0.02 s in Figure 6 as the initial condition, the forced 1L and 1T mode cases were calculated. Complete pressure histories under quasi-steady regions are shown in Figure 7.

The acoustic amplitude of PCCdyn2 is calculated from the bandpass filtered power spectral density for the 1L, and high-pass filtered power spectral density for the 1T. These post-processing methods are the same as for the experiments. The amplitudes are 0.20 MPa between 3441 and 3541 Hz for the 1L mode, and 0.77 MPa above 4545 Hz for the 1T. This is higher than the 1L and 1T amplitudes obtained in the experiment of 0.081 and 0.37 MPa, respectively. Because the boundary condition in the LES simulation is switched abruptly between open and closed, the mass flow modulation of the outflow is not smooth like in the experiment, and a strong pressure wave is generated. Comparing with the experimental data, the numerical amplitudes are around 147% for 1L and 108% for 1T. The average pressures of the 1L case is 6.16 MPa and the 1T case is 6.22 MPa, which are slightly higher than the corresponding experimental values. This is also considered to be the influence of the siren excitation boundary condition in the LES simulation.

4.1.3. Detailed comparison by mode shape evolution

Before comparing the numerical and experimental results for the excited cases, some explanation of the acoustic response observed in the BKH experiment is required.

The acoustic response over the course of the test with excitation is shown in Figure 8. Plotted are the signal amplitudes from each of the sensors, obtained using the Hilbert-Huang transform of the signals after band-pass filtering around the evolving excitation frequency with a bandwidth of 100 Hz. The amplitude of the 1L mode is maximum at the peak response frequency (f_{R1L_exp}) of 3288 Hz and the 1T peak response frequency (f_{R1T_exp}) is 4450 Hz.

The relative amplitudes measured at each sensor location, together with relative phase information also provided by the Hilbert-Huang transform, can be used to produce a two-dimensional reconstruction of the acoustic pressure distribution in the combustion chamber according to the procedure described by Beinke et al. [24,25]. The reconstructed pressure field in the combustion chamber is displayed for several frequencies from below to above f_{R1L_exp} and f_{R1T_exp}. These snapshots illustrate how the mode distribution evolves as the forcing frequency (f_{ex}) approaches and passes through the mode frequencies.

(a) symmetric response

A further aspect of the acoustic response in BKH to be considered is the asymmetric amplitude response of the 1T mode. The resonance frequency of the 1T mode is observed to increase during transverse forcing, resulting in a f_{R1T_exp} up to

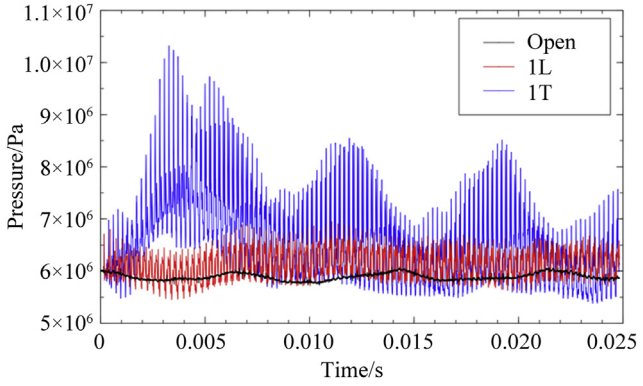

Figure 7 Pressure histories of all acoustic cases.

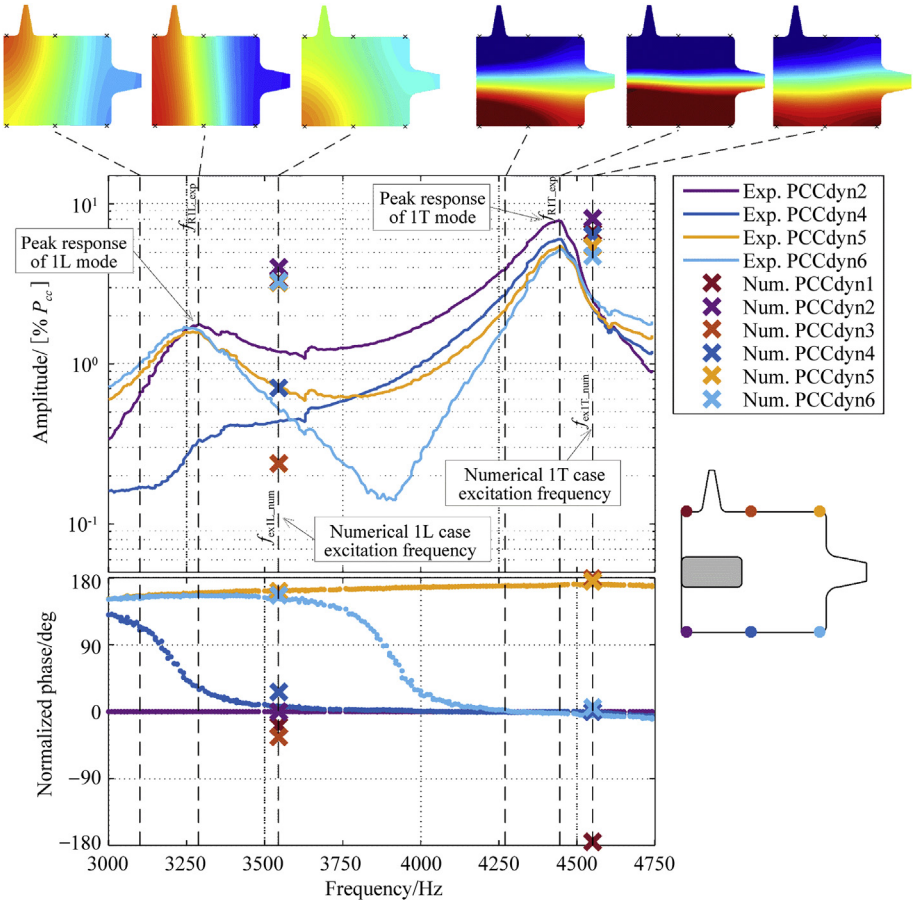

Figure 8 Acoustic response from a BKH test with ramped acoustic excitation.

5% higher than the unforced value (f_{01T}) [14,26,27]. In Figure 8, this manifests as a skew of the 1T response peak toward higher frequencies, with a shallower approach flank on the lower frequency side of f_{R1T_exp} and a steeper drop off on the higher frequency side. A recent study [27] used a low-order model to show that this effect can most likely be attributed to the response of the flames to the transverse acoustic velocity perturbation. The flames decrease in length causes a change in the speed-of-sound distribution in the combustion chamber which increases f_{01T}. When passing above f_{R1T_exp}, there is a quickly changing amplitude response and acoustic mode distribution as the flame recovers from the diminishing perturbation intensity and f_R relaxes back down to its unexcited value away from the continuously increasing f_{ex}. No such flame response to 1L mode excitation is observed in BKH, and so f_{R1L_exp} is similar in value to f_{01L} and the response peak is approximately symmetric.

(b) LES model response

The amplitude response from the LES model for the 1L and 1T excited cases is overlaid on Figure 8. The 1L response from the six probe locations appears at the applied f_{ex} of 3544 Hz, and the 1T response at 4551 Hz. In the amplitude plot it is immediately evident that the values of f_{ex} applied in the model do not correspond to f_0 in the experiment, and that the response amplitude in the model is greater than in the experiment. The greater amplitude is attributed to the hard excitation boundary condition applied to the secondary nozzle opening which results in forcing amplitudes greater than in the experiment.

(c) Identify equivalent response

The following approach was used to compare the equivalent responses from the experiment with those obtained in the two simulations. The amplitudes of both the experimental and numerical results were normalized to the amplitude at sensor PCCdyn2. These are displayed for the 1L mode on the left of Figure 9 and for the 1T mode on the right of Figure 9. Vertical dashed lines in Figure 9 indicate f_{R1L_exp} and f_{R1T_exp}. The distribution between sensor amplitudes now has a common scale for the experimental and numerical results.

As explained above, the acoustic field distribution inside the BKH chamber changes as the excitation frequency varies. An ordinary least squares regression method was used to determine which experimental frequency exhibited the most similar acoustic distribution to the model results. The least squares residual was computed as the sum of the square of the difference between the experimental and model normalized dynamic pressure sensor amplitudes at all

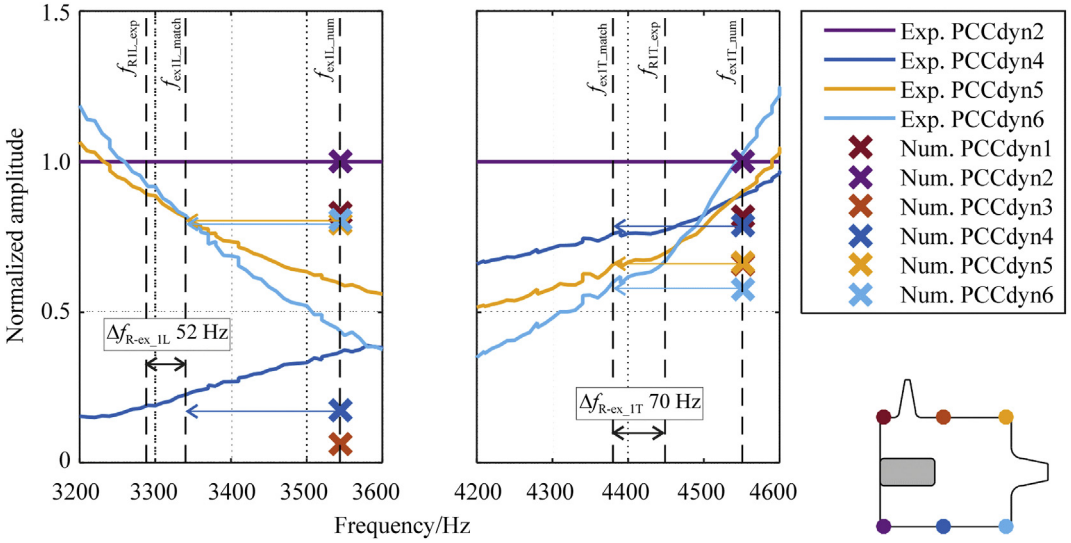

Figure 9 Normalized amplitude response for the 1L mode (left) and 1T mode (right) cases.

sensor positions for each excitation frequency. The minimum value of the least squares residual indicated the frequency at which the relative normalized amplitudes between sensor positions best matched the model results. This analysis found that the acoustic pressure distributions of the experiment and the model best matched for the 1L and 1T modes at frequencies of 3340 Hz and 4380 Hz, respectively. The arrows in Figure 9 indicate at which frequency the acoustic response of the model and experiment best match. For the 1L mode, this frequency is 52 Hz higher than f_{R1L_exp}, and for the 1T mode, the match is at a frequency 70 Hz below f_{R1T_exp}.

(d) Assessment of agreement

This exercise identified the closest match of relative acoustic amplitudes between sensor locations in the numerical and experimental data which gives insight into the relationship between f_{ex} and f_R in the simulation. The agreement between the modal distribution in the simulation

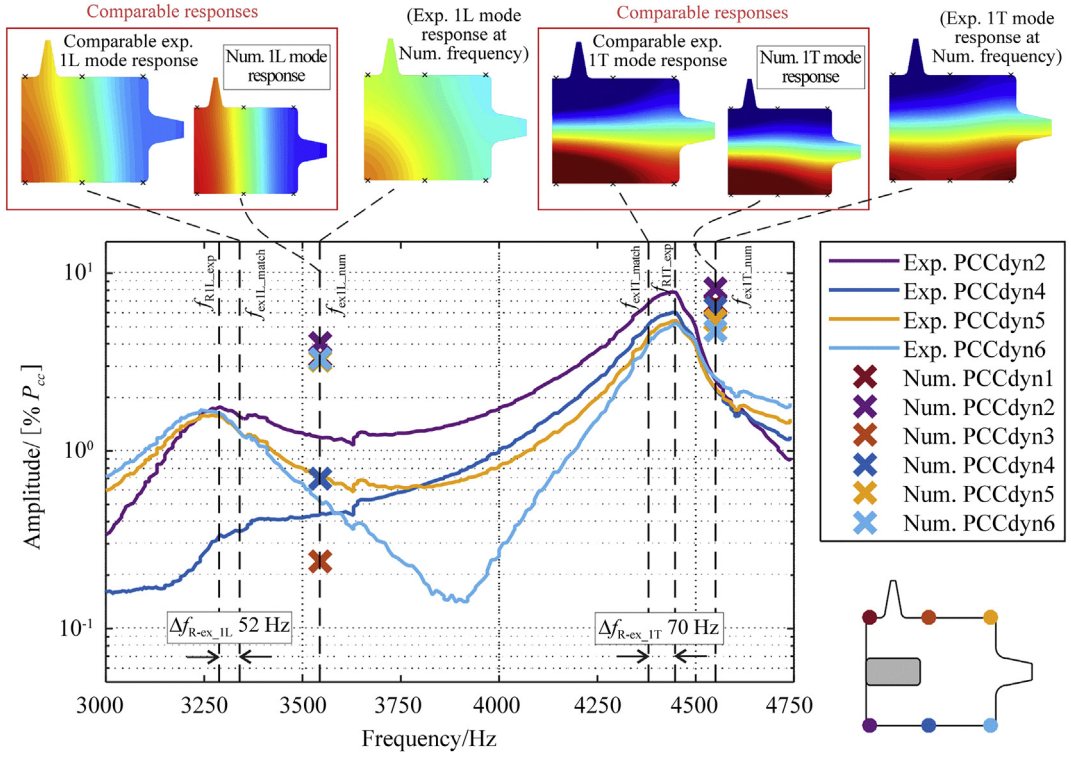

Figure 10 Comparison of acoustic pressure distributions from experiment and simulation at equivalent acoustic response frequencies.

and the equivalent distribution at the matched experimental frequency is very good. For the 1L mode, the ordinary least squares residual (OLSR) of 0.003 is nearly two orders of magnitude lower than at the actual simulation frequency of 3544 Hz. For the 1T mode, the OLSR of 0.001 is more than two orders of magnitude lower than at 4551 Hz. This can also be illustrated qualitatively in Figure 10, where the 'equivalent' response distributions from model and experiment are reconstructed and compared. Note that the pressure fields in this subsection have been reconstructed by the signals from each sensor in the CFD result, as done in the experiments, i.e., the pressure fields are not the same as the fields obtained by CFD simulations. The overall good agreement indicates that the model captures the acoustic response of the experiment well.

It is also noteworthy that the match between the 1T mode response in the simulation and the experiment indicates a f_{R1T_exp} higher than f_{01T} in the simulation. This is consistent with the asymmetric acoustic response observed in the experiment due to flame retraction under transverse acoustic forcing, and therefore suggests that the model is also able to reproduce this phenomenon. This ability will later be confirmed in this work through the consideration of optical imaging of the flame response in BKH.

4.2. Average flame topology

In this section, the structure of the flame by the LES simulations will be compared with that observed in the experiment with shadowgraph imaging. The topology of the flame in a time-averaged sense will first be assessed, followed by analysis of the mechanism of LOx jet shortening in the 1T case.

A qualitative comparison of the average flame topology for the three cases is presented in Figure 11. The comparison is based on the interpretation of intensity gradients in time-averaged shadowgraph images from the experiment, which have been established in past work to represent the boarders of the dense oxygen jets and features of their breakup [10,14]. Shadowgraph images averaged over a time span of 100 ms are shown in the left-hand column of Figure 11. Features relevant to the topology of the dense oxygen jets are traced in blue in order to highlight them and to overlay them on a comparable result from the simulation.

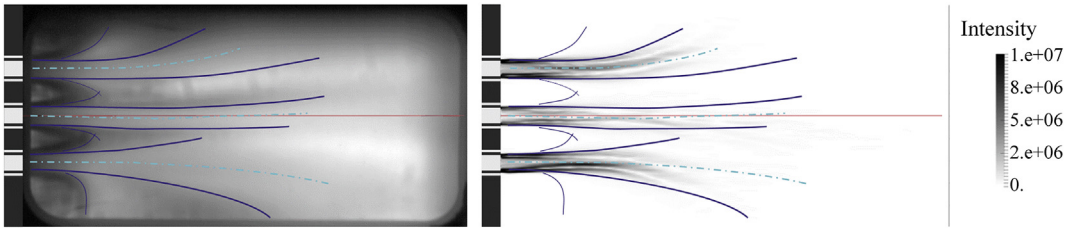

(a) Unexcited case (Left: Experimental shadow graph, Right: LES pseudo-shadow graph)

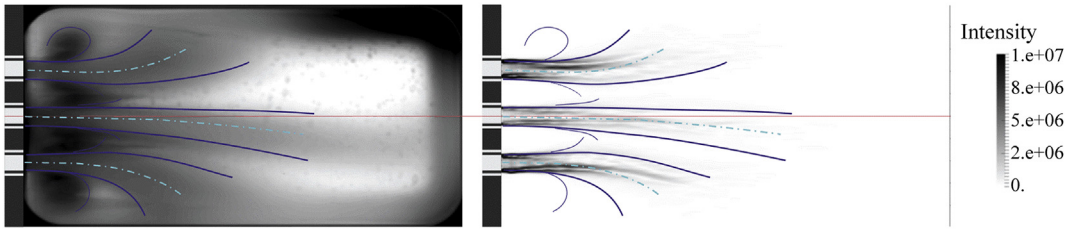

(b) Excited 1L mode (Left: Experimental shadow graph, Right: LES pseudo-shadow graph)

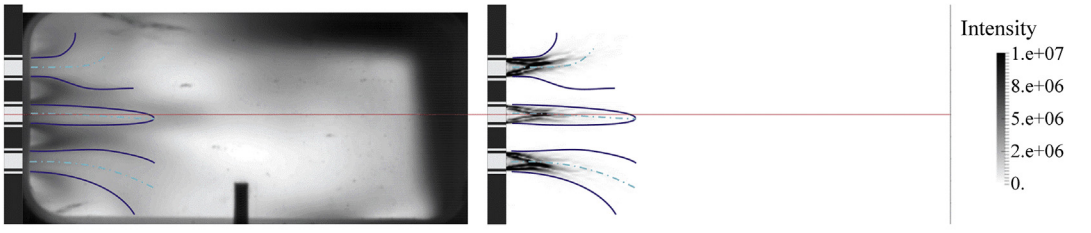

(c) Excited 1T mode (Left: Experimental shadow graph, Right: LES pseudo-shadow graph)

Figure 11 Comparison of mean flame topology. (a) Unexcited case (Left: Experimental shadow graph, Right: LES pseudo-shadow graph). (b) Excited 1L mode (Left: Experimental shadow graph, Right: LES pseudo-shadow graph). (c) Excited 1T mode (Left: Experimental shadow graph, Right: LES pseudo-shadow graph).

This comparable numerical result, displayed in the right-hand column of Figure 11, is a pseudo-shadowgraph image produced by performing a Laplacian to density on *xy*-plane and integrating the results along the *z*-direction. Note that refraction and diffraction of light is not taken into consideration. The images shown here are the average from a time span of around 20 ms. Longer image sequences of a duration approaching that of the experimental data were not obtained in the output of the simulation, so the comparability with the time-averaged images from experiment is limited.

Notwithstanding this limitation, several points of similarity can be identified by considering the overlay of traced features on the pseudo-shadowgraph images. Beginning with the unexcited case in Figure 11(a), the course of the centerlines of the three visible LOx jets, shown as green dashed lines within the figure, is matched well in the simulation. The outer jets begin to deflect noticeably outwards from about 30 mm downstream of injection, outlined by the thick blue lines, and this outward deflection is captured by the model. Due to the dynamic nature of the natural breakup mechanism, the appearance of the jet becomes smeared with increasing downstream distance, and no clear end of the jet can be identified. The boarders of the jet are no longer clearly discernible from about 60 mm downstream, which is where the tracing ends. This extent of the discernible intact core of the LOx jet appears to be captured well in the pseudo-shadowgraph of the simulation. All jets exhibit diffuse expansion of material away from the central jet approximately 20 mm downstream of the injection plane in Figure 11(a), traced by thin blue lines. These features are not identifiable in the pseudo-shadowgraph from the simulation.

The 1L case in Figure 11(b) appears qualitatively much the same as the unexcited case. In a time-averaged sense the mean paths and breakup of the LOx jets are

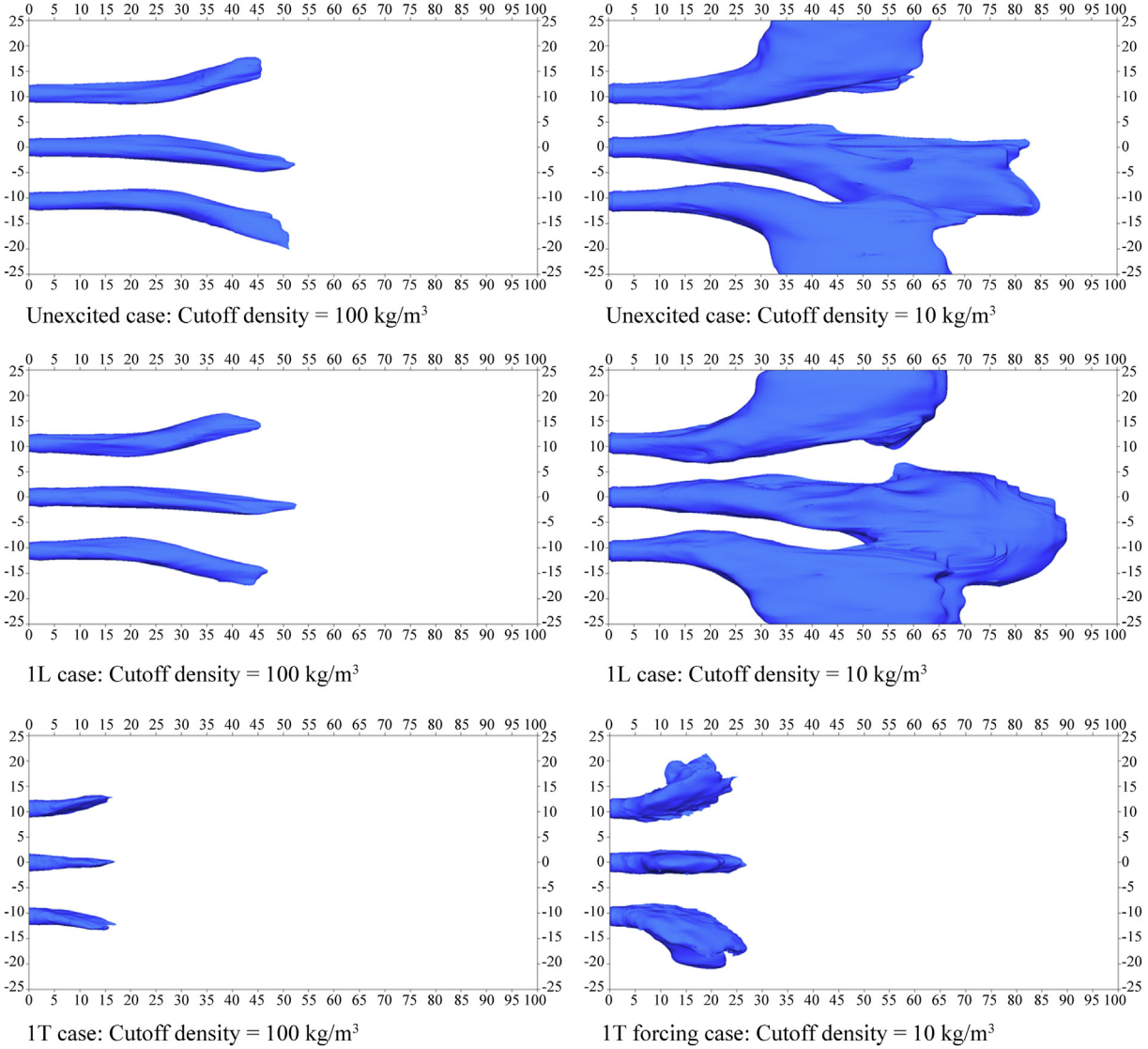

Figure 12 Comparisons of LOx core length of three cases.

apparently undisturbed by the excited longitudinal chamber mode.

The 1T case in Figure 11(c) exhibits significant differences to the unexcited and 1L cases, reflecting the strong response of the LOx jets to transverse acoustic velocity. As explained in previous work [9,14], the intact part of the LOx jets shortens as the breakup is driven by accelerated stripping and entrainment of oxygen from the jet surface into the oscillating transverse acoustic flow. The intact part of the central jet tends to remain steady under this mechanism, and so its boundaries and extent can be clearly identified in the time-averaged shadowgraph image. The outward deflection of the upper and lower jets also increases under the 1T mode perturbation. These three features - the form and length of the central jet and the increased deflection of the outer jets - are captured well in the simulation.

4.3. *Summary of comparison, link to acoustic response*

The shortening of the LOx jets seen in Figure 11(c) for the 1T case is accompanied by a shortening of the extent of the flame and increased density of energy release in the upstream part of the combustion chamber [9,14]. This is believed to be responsible for the asymmetric acoustic response of ramped excitation of the 1T mode, as discussed previously in Section 4.1.3. The good agreement between the response of the LOx jets in the experiment and the simulation explains why the model could reproduce the acoustic field distribution in the combustion chamber so well. In all, the model is able to reproduce well features of the flame topology and its acoustic response as described in shadowgraph imaging.

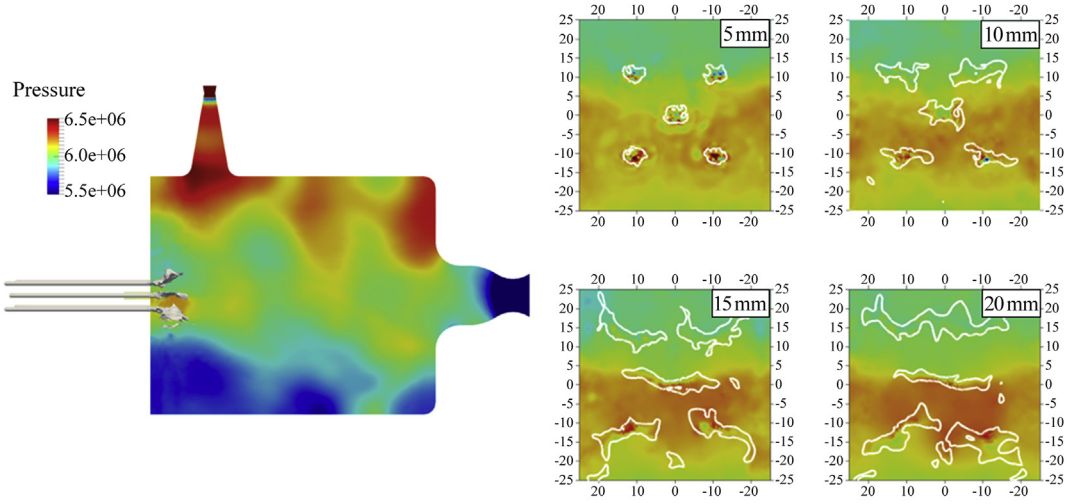

(a) 1T mode: Phase = 0

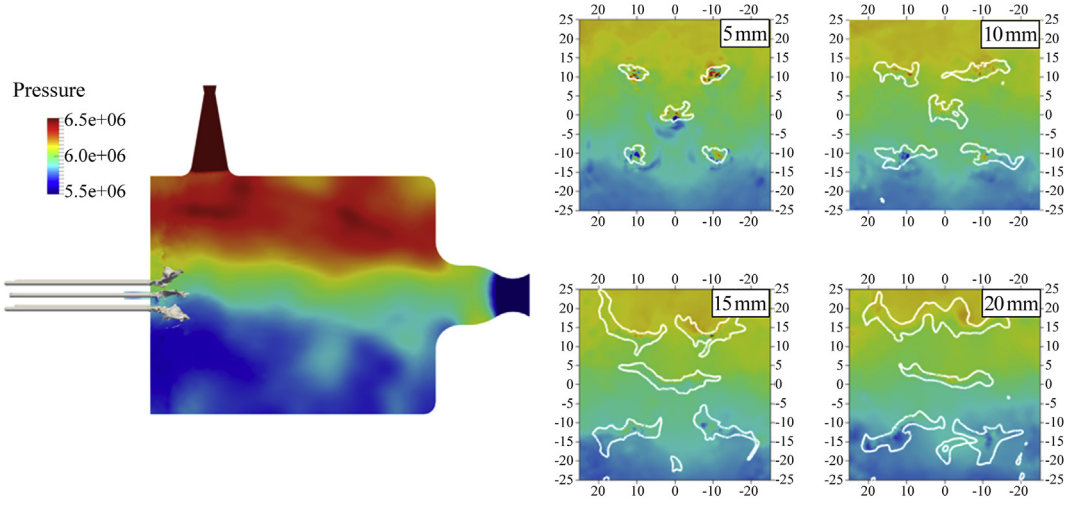

(b) 1T mode: Phase = 1/4π

Figure 13-1 Pressure fields and iso-surface of density at 10 kg/m^3 for 1 acoustic cycle between 16.07 and 16.29 ms, at cross-sections located 5, 10, 15, and 20 mm from the injection plane. (a) 1T mode: Phase = 0. (b) 1T mode: Phase = 1/4π.

4.4. Acoustic velocity response

It is difficult to judge the length of the LOx core in the pseudo-shadowgraph images obtained from the numerical simulation. Iso-surfaces of density are found to be more appropriate for determining core length. Figure 12 shows density iso-surfaces for determining the LOx core length in the three cases. There is no way to relate structures discerned in the experimental shadowgraph images to specific values of oxygen density, so a trial-and-error approach was adopted. The left column of Figure 12 shows iso-surfaces of 100 kg/m^3, and the right column of 10 kg/m^3, averaged over 20 msec. These density values were chosen so that the effects of the siren were clear.

Based on a qualitative comparison with the shadowgraph imaging in Figure 11, it is estimated that the density of the experimentally observed LOx core lies between 10 and 100 kg/m^3. From now on, the length of the LOx core in the numerical simulation will be defined by density iso-surfaces of 10−100 kg/m^3.

In Figure 12, the numerical results in the 1L case are qualitatively the same as the open case in terms of LOx core length and shapes. However, the length of the LOx core is shortened and flattened in the 1T case. To discuss the 1T case in detail, Figure 13 shows the pressure field and density for one cycle in every quarter cycle. The result shows that the LOx core is greatly flattened and spread as it extends downstream. The Strouhal number is $St = f_{1T}D_{LOx}/u_{LOx} = 1.31$. From the results of Gonzalez-Flesca et al. [13], it is difficult to distinguish the effect of velocity fluctuation on the LOx core with high St. Indeed, from the instantaneous pressure fields and density traces at the planes at $x = 5-20$ mm, it is difficult to distinguish variation at the edge of the LOx core. To clarify the density fluctuation, the one-cycle average RMS of the density fluctuation are shown in Figure 14. From the RMS distribution it is confirmed that the edge of the LOx core has

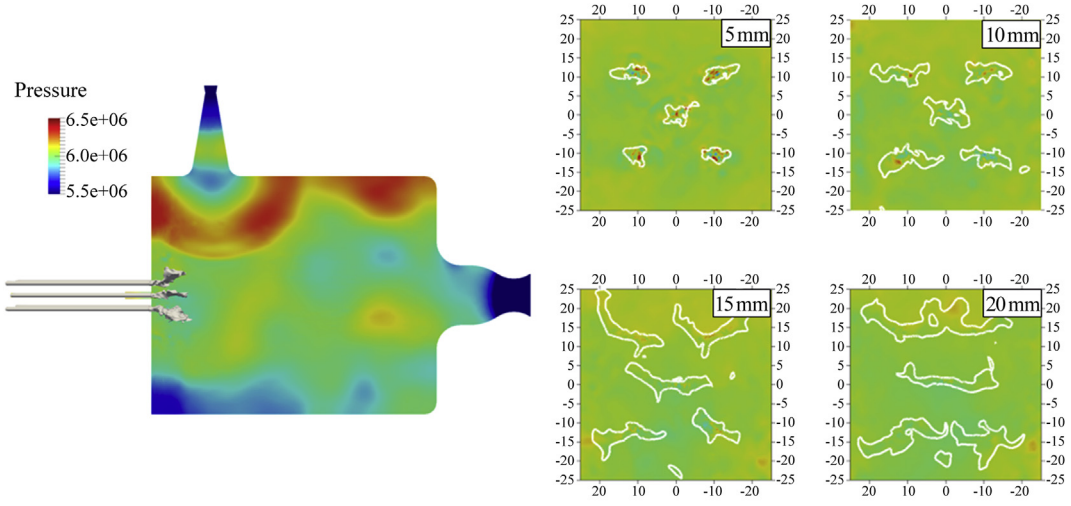

(c) 1T mode: Phase = 1/2π

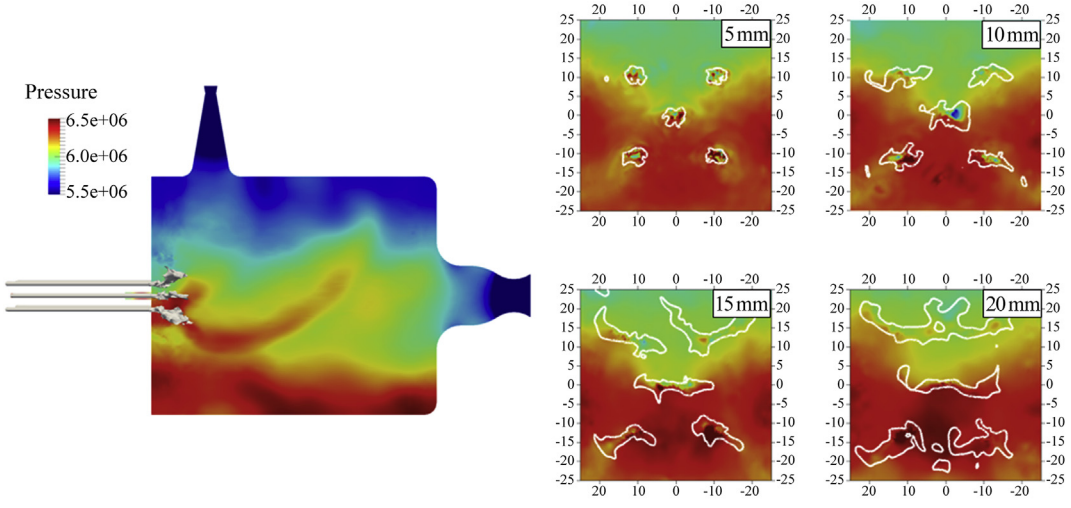

(d) 1T mode: Phase = 3/4π

Figure 13-2 Pressure fields and iso-surface of density at 10 kg/m^3 for 1 acoustic cycle between 16.07 and 16.29 ms. (c) 1T mode: Phase = 1/2π. (d) 1T mode: Phase = 3/4π.

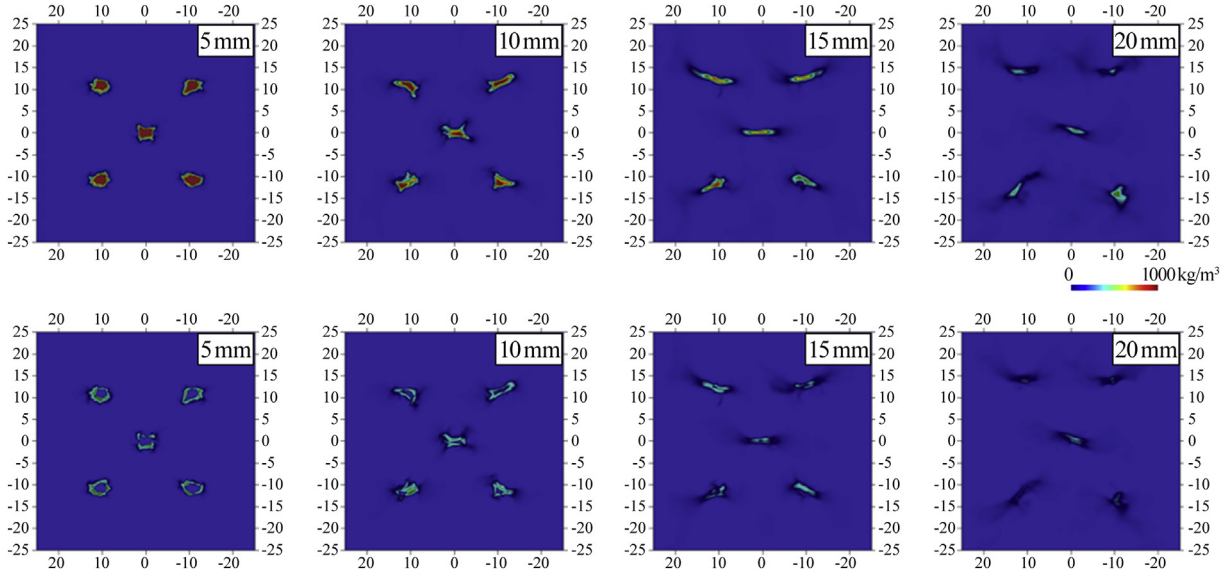

Figure 14 Cross-sections of one-cycle averaged density (upper row) and RMS of density (lower row) at $x = 5-20$ mm.

large fluctuations, and the low-density LOx here moves under the influence of acoustic velocity. Later, we will explain the shape of the LOx core in a forced 1T case.

As explained earlier in section 4.1.3(b), the boundary condition of the secondary nozzle in the LES simulation produces a strong pressure wave, so the pressure amplitude is higher than in the experimental data. Therefore, a second excited 1T mode case ($1T_2$) was carried out in order to obtain a lower pressure amplitude than in the original 1T case ($1T_1$). Numerical experiments have shown that increasing the secondary nozzle closing time, i.e., the period during which the boundary condition of the secondary nozzle was the slip wall condition, decreases the pressure amplitude and velocity fluctuation. This is because the mass flow rate of the secondary nozzle greatly depends on the closing time. Therefore, the $1T_2$ case was run with a nozzle closing time of 1.75 times that of $1T_1$. Note that the times shown in Figures 15 and 16 were the times when the results were quasi-steady states. For the case of $1T_2$, it cost more time to be stable compared to the case $1T_1$. Therefore, the times for Case 1 and Case 2 were different.

The velocity histories and one-cycle averaged iso-surface of density of the $1T_1$ and $1T_2$ cases are shown in Figures 15 and 16, respectively. In Figure 15, the velocity amplitude of the $1T_2$ case is smaller compared to the $1T_1$ case, as desired. In addition, in Figure 16, the averaged iso-surface of the density in the $1T_2$ case becomes longer compared with the original $1T_1$ case.

Core length measurements from Hardi et al. [10] are shown in Figure 17. The set of points included are from BKH tests with operating conditions corresponding to those of the current test case, namely at a combustion chamber pressure of 6 MPa with ambient hydrogen injection temperature (T_{H_2}). Intact core length values (L) are normalized by the inner diameter of the oxygen injector, or 'LOx post' (D). The acoustic pressure amplitude is estimated by multiplying the RMS of the dynamic pressure signal from PCCdyn2 by the square root of 2. While in Refs. [10] the

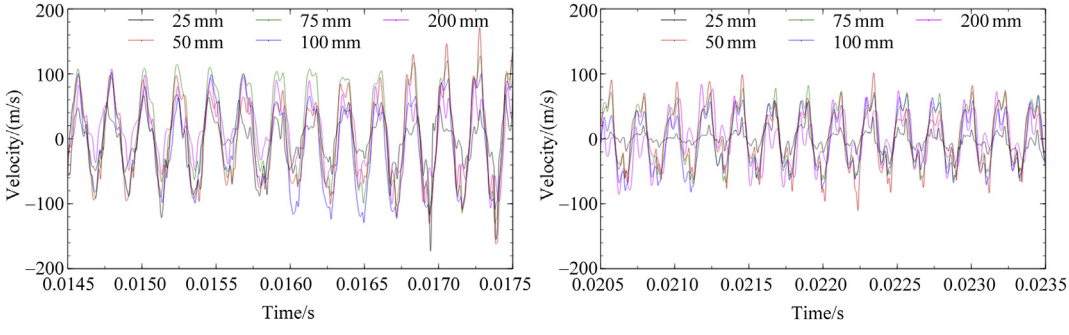

(a) Case $1T_1$ (b) Case $1T_2$

Figure 15 v-velocity histories at $x = 25-200$ mm, $y = 0$ mm, and $z = 0$ mm. (a) Case $1T_1$. (b) Case $1T_2$.

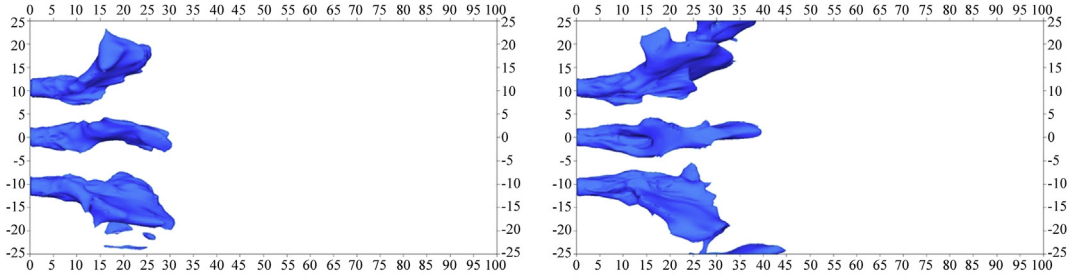

(a) Case $1T_1$ (16.07 - 16.29 ms) (b) Case $1T_2$ (22.26 - 22.47 ms)

Figure 16 One-cycle averaged iso-surface of density at 10 kg/m^3. (a) Case $1T_1$ (16.07−16.29 ms). (b) Case $1T_2$ (22.26−22.47 ms).

dynamic pressure signal was first high-pass filtered to include all acoustic content, here the signal was band pass filtered around the 1T mode response. This way, the value represents the contribution to the pressure amplitude which corresponds to the velocity amplitude of the 1T mode at the centerline of the combustion chamber. The experimental and numerical results were treated the same way. Pressure amplitude is normalized by mean combustion chamber pressure (P_{cc}).

On the upper horizontal axis, the acoustic velocity amplitude (u') at the axis of the chamber is displayed. It is estimated using $u' = p'/\rho c$, assuming an ideal 1T mode distribution and using values of ρ and c for the bulk equilibrium mixture in the combustion chamber calculated with CEA [28]. The local values of ρ and c around the central LOx jet may differ from the bulk values, and with them the estimated value of velocity amplitude. Therefore, the velocity amplitude scaling on the upper axis is given for reference purposes only.

The intact length of the central LOx jet from the LES of the $1T_1$ and $1T_2$ cases are overlaid on the experimental data set in Figure 17. The error bars represent the range of maximum core length measured from the density iso-surface of 10 kg/m^3 to minimum core length for the density iso-surface of 100 kg/m^3, averaged for one cycle. The $1T_1$ point lies at an L/D of 8.5 and amplitude of 7.36%, slightly higher than the maximum amplitude reached in the experiment. To assist the comparison, an exponential curve was fit to the data set and extrapolated beyond the amplitude of the LES result. The LES result lies only 0.56 L/D above the extrapolated experimental result, and the vertical error bars describing the uncertainty in the intact core length encompass the extrapolation. The error bars for the $1T_2$ point at $L/D = 9.7$ also encompass the fit curve. Therefore, the LOx core response in the model can be said to match the experimental observation well.

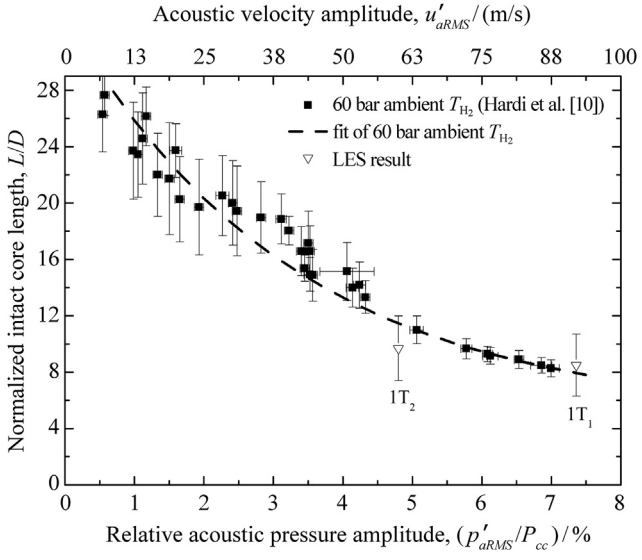

Figure 17 Length of intact LOx core vs. acoustic pressure amplitude of the 1T mode.

4.5. Acoustic pressure response

The effects of velocity and pressure fluctuations for conditions representative of the experimental test case have so far been presented. However, the excitation of the 1L mode (pressure fluctuation) in the experiment is weaker than for the 1T mode (velocity fluctuation). Therefore, numerical experiments were conducted for the 1L case with stronger pressure amplitude. A siren boundary condition similar to that for the secondary nozzle was developed for the main nozzle in order to excite the 1L mode more effectively. At the center of the main nozzle, an obstacle with 15% of the area of the main nozzle was set as a wall boundary with siren forcing. The resulting histories of pressure and u-velocity, and density iso-surfaces of this $1L_2$ case are compared with the original 1L case in Figure 18. The pressure at PCCdyn2 is around 1.5 MPa, and the velocity amplitude at (x, y, z) = (0.1, 0, 0) is around 300 m/s. These fluctuations in pressure and u-velocity are much greater than in the original 1L ($1L_1$) and even 1T cases. However, in the density iso-surfaces in Figure 18, the length of the LOx core is only slightly shorter in the $1L_2$ case because the u-velocity fluctuation is parallel to the jet and only reaches significant amplitudes from around x = 55 mm. Thus, it can be concluded that the influence of transverse velocity fluctuations on the flame is the most important for flame shortening.

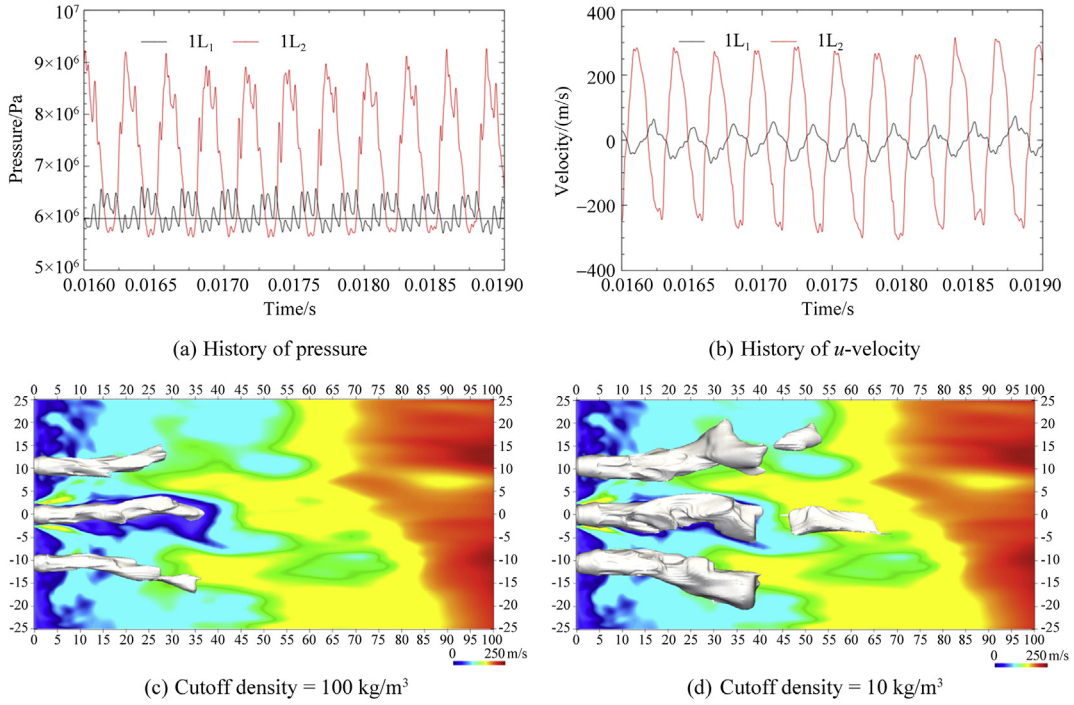

(a) History of pressure

(b) History of *u*-velocity

(c) Cutoff density = 100 kg/m^3

(d) Cutoff density = 10 kg/m^3

Figure 18 Pressure history at PCCdyn2 and velocity history at $(x, y, z) = (0.1, 0, 0)$ (upper row) and iso-surfaces of density with a background of *u*-velocity fluctuation amplitude for 1 cycle (below) between 17.48 and 17.76 ms. (a) History of pressure. (b) History of *u*-velocity. (c) Cutoff density = 100 kg/m^3. (d) Cutoff density = 10 kg/m.^{3}.

4.6. *Mechanism of LOx core shortening and flattening*

The mechanism of LOx core shortening will now be explored in more detail. Distributions of pressure and *v*-velocity fluctuation for the unexcited, 1L, and 1T$_1$ cases are shown in Figures 19—21, respectively. In Figures 19 and 20, there are only slight differences in the velocity fluctuations between the unexcited and 1L cases. The velocity fluctuation is larger in the 1L case because the pressure wave propagates with a component in the *y*-direction when the 1L mode is excited by the secondary nozzle. In the 1T case in Figure 21, the *v*-velocity fluctuations are strong in

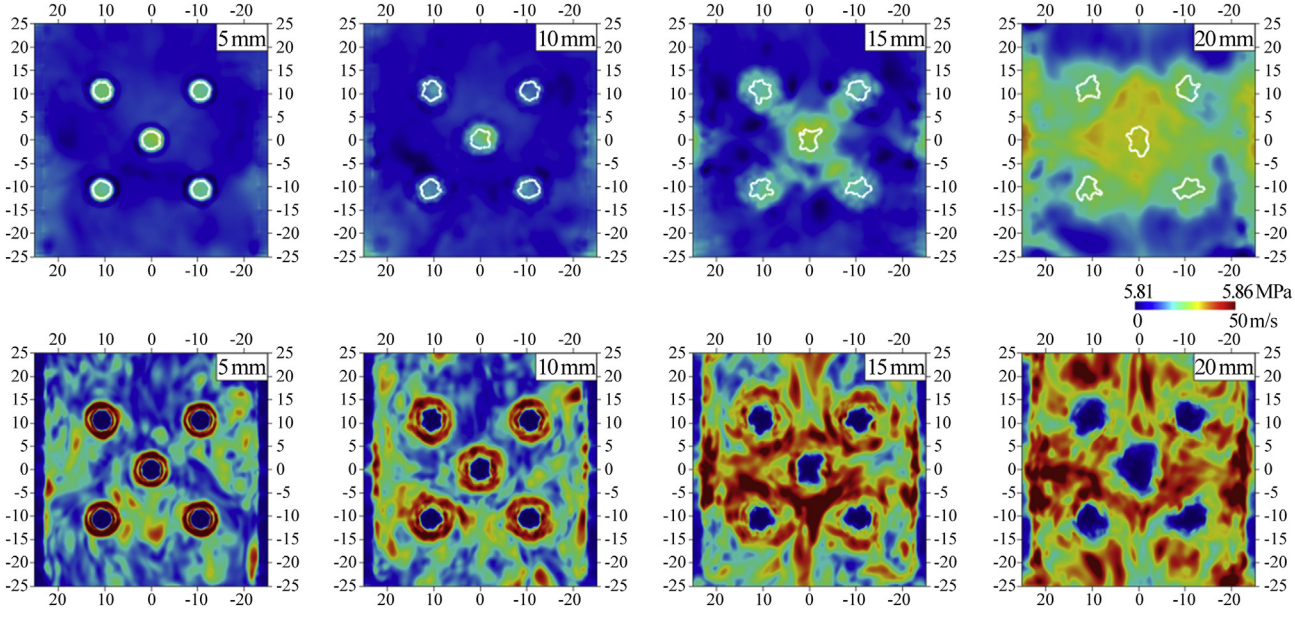

Figure 19 Cross-sections of pressure (top) and *v*-velocity fluctuation (bottom) for the unexcited case. The white contour line is for a density of 100 kg/m^3 averaged between 16.07 and 16.35 ms.

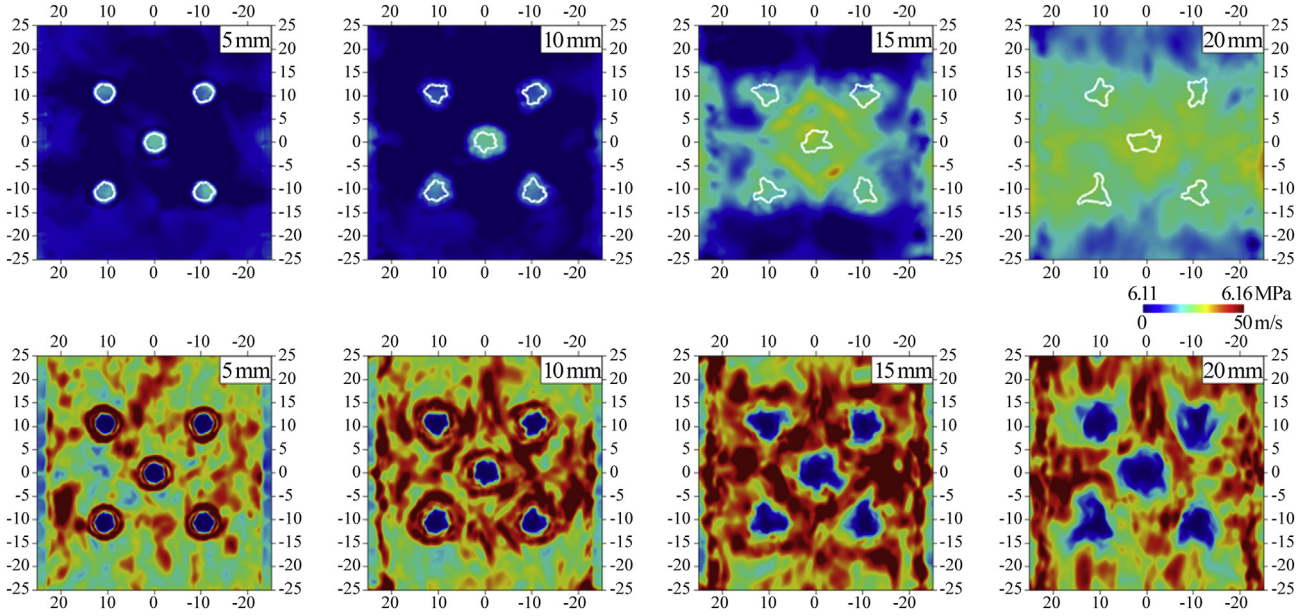

Figure 20 Cross-sections of pressure (top) and *v*-velocity fluctuation (bottom) for 1 cycle of the 1L case. The white contour line is for a density of 100 kg/m^3 averaged between 16.07 and 16.35 ms.

accordance with the 1T mode distribution. At the edges of the flattening LOx core, the pressure is lower compared to the upper and lower regions.

The role of this pressure distribution on LOx core shortening has been explained by Hakim et al. using Bernoulli's theorem [11]. Hakim et al. reported that, as the velocity around the LOx core increases, the pressure decreases and the core is stretched sideways, which also shortens it. The pressure drop at the sides of the core in the LES result in Figure 21 is ΔP: -14.2×10^3 Pa. The coordinates used for comparison are $(x, y, z) = (15, 0, -10)$ and $(15, 2.5, 0)$. The value obtained from theory as presented by Hakim et al. at these points is -15.6×10^3 Pa. The reason for a lower pressure drop in the LES than the theoretical value is that the surface of the LOx core does not work sufficiently as a cylindrical rigid wall. Furthermore, the density decreases with increasing downstream distance.

Notwithstanding the limitations of applying Bernoulli's theorem to a non-rigid surface, the theory of Hakim et al. has been extended to take into account the divergence of the

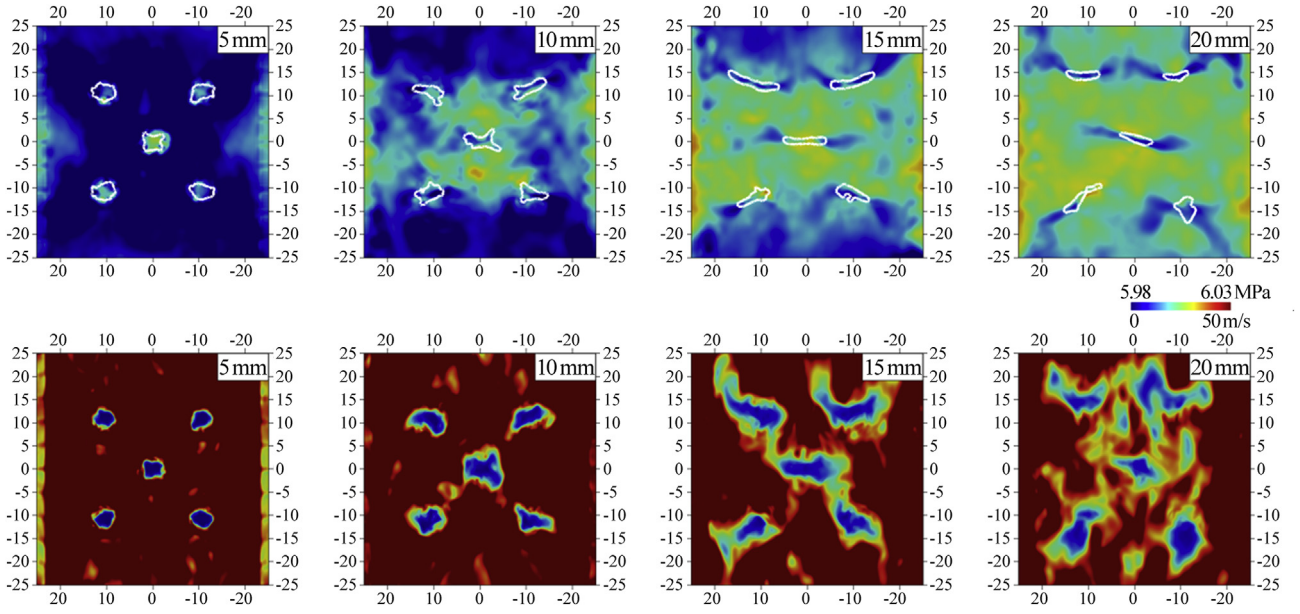

Figure 21 Cross-sections of pressure (top) and *v*-velocity fluctuation (bottom) for 1 cycle of the 1T case between 16.07 and 16.29 ms. The white contour line is for a density of 100 kg/m^3.

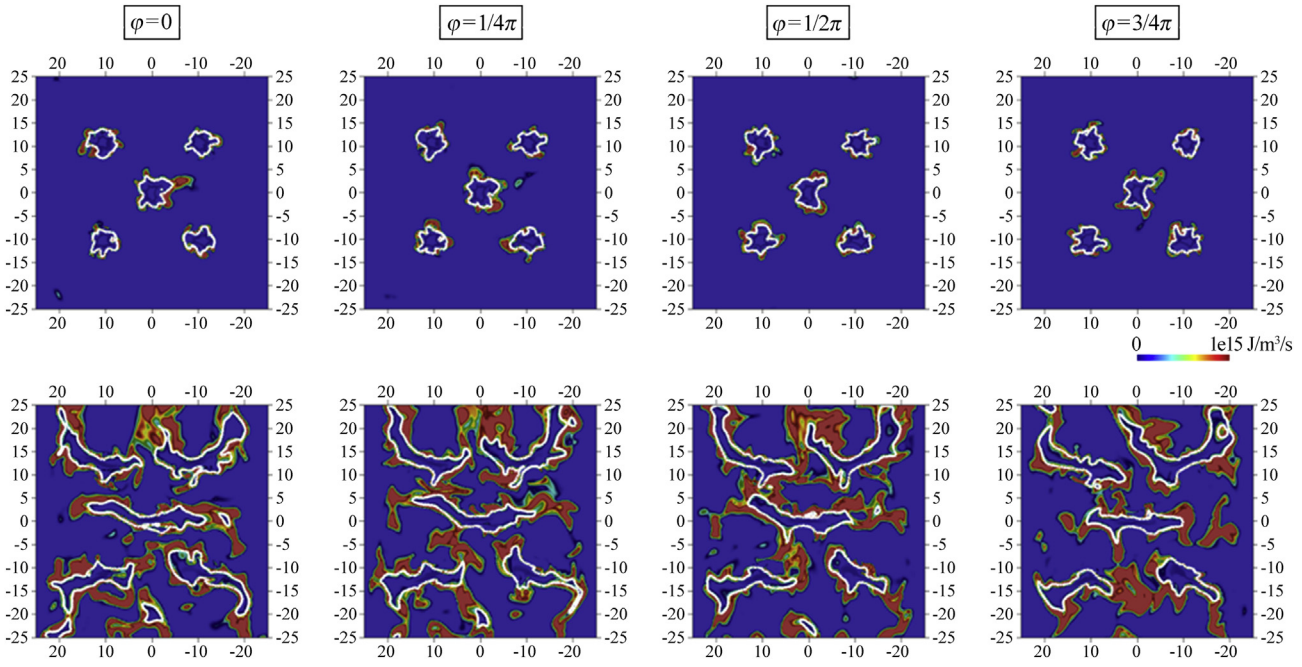

Figure 22 Cross sections of heat release rate for the unexcited (upper row) and 1T cases (lower row) at $x = 15$ mm. The snapshots from left to right are at quarter-cycle intervals for one cycle between 16.07 and 16.29 ms. The white contour line is for a stoichiometric mixture fraction of 0.111.

LOx core from a simple cylinder. The theory uses elliptical forms to approximate the flattening of the core under the influence of transverse velocity fluctuations, and is presented in the Appendix. This approach is used to determine the pressure profile for the LOx core as it flattens steadily with increasing axial distance. As would be expected, the elliptical shape increases the v-velocity at the major axes of the LOx core, and the pressure drop further increases. Thus, the tendency to further flattening occurs.

To further elaborate on the LOx core shortening mechanism for the 1T case, Figure 22 shows the heat release rate and density over one cycle at every quarter cycle for the unexcited and 1T cases. The heat release rate was calculated by the dot-product of the rates of progress and the molar enthalpies obtained from the instantaneous field of the mass fractions. Compared to the unexcited case, the surface area of the flame is much larger in the 1T case because of the LOx core spreading. This results in a greater heat release rate which reflects the accelerated consumption of propellants, also contributing to LOx core shortening.

5. Conclusions

High pressure H_2/O_2 rocket flame response under acoustically excited states was studied experimentally and numerically. The configuration studied was the DLR experimental combustor BKH, with five injection elements, optical access, and an acoustic excitation system. Experimental and numerical data sets were compared on the basis of combustion chamber acoustics and visualization of flame topology.

The boundary conditions of the numerical model cause the acoustic conditions within the combustion chamber to differ from those in the experiment. A method was developed to compare the equivalent acoustic response of the simulation to the experiment, although the frequencies and amplitudes of the resonance modes differed. The resulting comparison showed good agreement, and indicates the ability of the model to recover the dynamic flame response to a forced acoustic field.

Flame topology was studied by visualizing the dense oxygen jet, or LOx core, of the shear coaxial injection elements with shadowgraph imaging in the experiment, and with density iso-surfaces in the simulation. It was found that the LOx core length became shorter under transverse (v-velocity) forcing, and that flame shortening did not occur under longitudinal (pressure) forcing. The mechanism for LOx core shortening under v-velocity perturbations was explored. The LOx core becomes shorter because it spreads and flattens in the direction perpendicular to the v-velocity. The transverse spreading and flattening could be explained by the pressure distributions from the numerical simulation. A previous explanation for the spreading using the unsteady Bernoulli's theorem has been expanded to use elliptical geometry to approximate the cross-sectional form of the jet under the influence of the v-velocity.

Acknowledgements

The experimental data were gathered with the assistance of Dmitry Suslov, Walter Clauβ, and the crew of the P8 test bench. This work was performed in the frame of the Franco-German Rocket Engine Stability iniTiative (REST), and the DLR-JAXA Joint Research Agreement on liquid propellant space propulsion. Research undertaken for this report has been assisted with a grant from the Sir Ross and Sir Keith Smith Fund (Smith Fund) (www.smithfund.org.au). The support is acknowledged and greatly appreciated. The Smith Fund by providing funding for this project does not verify the accuracy of any findings or any representations contained in it. Any reliance on the findings in any written report or information provided to you should be based solely on your own assessment and conclusions. The Smith fund does not accept any responsibility or liability from any person, company or entity that may have relied on any written report or representations contained in this report if that person, company or entity suffers any loss (financial or otherwise) as a result.

Appendix. Pressure drop around an elliptical cylinder

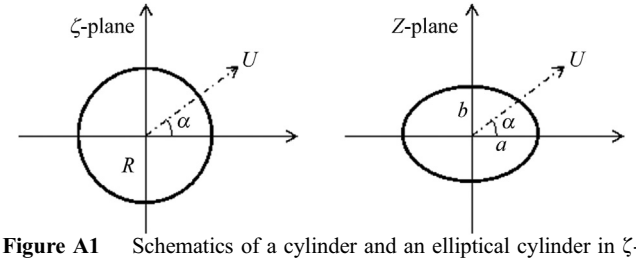

Figure A1 Schematics of a cylinder and an elliptical cylinder in ζ- and Z-plane respectively.

In this appendix, the flow field around an elliptical cylinder is derived by Joukowski transformation of the flow around a cylinder to calculate the pressure drop around the elliptical cylinder.

The flow field around a cylinder is represented in a complex plane ζ, and the flow field around the elliptical cylinder to be obtained is denoted by plane Z (Figure A1). Complex velocity potential around the cylinder can be written as $W = U\left(\zeta\exp(-i\alpha) + \frac{R^2\exp(i\alpha)}{\zeta}\right)$, where R is radius, U is the uniform velocity with angle α in ζ-plane. Joukowski transformation is defined $Z = \zeta + \frac{A^2}{\zeta}$. Then the flow around the elliptical cylinder with the axes a, b (corresponds to major and minor axis respectively) can be written as $W = \varphi + i\Psi = U\left(\frac{\exp(-i\alpha)}{2}(\sqrt{Z^2-4A^2}+Z) + \frac{2\exp(i\alpha)R^2}{\sqrt{Z^2-4A^2}+Z}\right)$, where $R = \frac{a+b}{2}$, $A = \frac{\sqrt{a^2-b^2}}{2}$, φ and Ψ are the real and imaginary parts of the velocity potential respectively. Then the velocity field is obtained by differentiation with Z,

$$\frac{dW}{dz} \equiv u - iv = U\left(\frac{\exp(-i\alpha)}{2}\left(1+\frac{Z}{\sqrt{Z^2-4A^2}}\right) - \frac{2\exp(i\alpha)R^2\left(1+\frac{Z}{\sqrt{Z^2-4A^2}}\right)}{\left(\sqrt{Z^2-4A^2}+Z\right)^2}\right).$$

Below, assuming $\alpha = \pi/2$ and we focus on the velocity field at the $(a, 0)$ coordinate point in the $Z = X + iY$ plane to evaluate the maximum pressure drop. For later use $a = \varepsilon c$ and $b = c/\varepsilon$ are set. After some computation, we have $\frac{\partial\varphi}{\partial t} = \frac{\partial}{\partial t}\mathrm{Re}(W) = 0$, $u = \mathrm{Re}\left(\frac{dW}{dz}\right) = 0$, and $v = -\mathrm{Im}\left(\frac{dW}{dz}\right) = U(1+\varepsilon^2)$.

When $\varepsilon = 1$ a well-known result for a circular cylinder is reproduced. (the velocity of the y component is $2U$). The velocity field does not depend on the size of the ellipse (c). The velocity of the y component increases as it becomes flat in the direction perpendicular to U.

The pressure drop is calculated based on the unsteady Bernoulli equation. $\frac{\partial\varphi}{\partial t} + \frac{p}{\rho} + \frac{\boldsymbol{u}^2}{2} = 0$, by substituting $\partial\varphi/\partial t$, u and v calculated above and replacing U as the actual acoustic velocity fluctuation, i.e., $U \to u_0\cos(2\pi ft)$, the pressure can be obtained as $p_{x=a,y=0} = -\frac{\rho}{2}\boldsymbol{u}^2\Big|_{x=1,y=0} = -\frac{\rho}{4}u_0^2\{1+\cos(4\pi ft)\}(1+\varepsilon^2)^2$, and $p_{x=\infty,y=0} = -\frac{\rho}{2}U^2 = -\frac{\rho}{4}u_0^2\{1+\cos(4\pi ft)\}$.

Thus, the pressure drop is obtained as $\Delta p = p_{x=a,y=0} - p_{x=\infty,y=0} = -\frac{\rho}{4}u_0^2\{1+\cos(4\pi ft)\}\{(1+\varepsilon^2)^2 - 1\}$.

When $\varepsilon = 1$, the results of Hakim et al. around the circular cylinder is reproduced ($-\frac{3}{4}\rho u_0^2$). At $\varepsilon = 1.3$ (corresponding to the shape expressed in Figure A1 right), the average pressure drop doubles ($-\frac{6.2}{4}\rho u_0^2$). Therefore, as the ellipse becomes flattened, the velocity around the ellipse increases, and the pressure decreases more on the left and right sides of the ellipse. This would enhance the additional flattening in the direction perpendicular to U (the direction of the acoustic velocity) observed experimentally and numerically.

References

[1] D. Watanabe, T. Tamura, T. Onga, H. Manako, N. Negoro, A. Kurosu, T. Kobayashi, K. Okita, Hot-fire testing of LE-X thrust chamber assembly, in: 30th International Symposium on Space Technology and Science (ISTS), Kobe, Japan, 2015.
[2] V. Yang, Liquid Rocket Engine Combustion Instability, AIAA, Washington, DC, 1995.
[3] F. Cheuret, Instabilités thermo-acoustiques de combustion haute-fréquence dans les moteurs fusées, Université de Provence Aix-Marseille, 2005.

[4] F. Richecoeur, Expérimentations et simulations numériques des interactions entre modes acoustiques transverses et flammes cryotechniques, École Centrale Paris, 2006.
[5] M. Oschwald, B. Knapp, Investigation of combustion chamber acoustics and its interaction with LOX/H_2 spray flames, in: L.T. DeLuca, C. Bonnal, O.J. Haidn, S.M. Frolov (Eds.), 2nd European Conference for Aerospace Sciences, Torus Press and EDP Sciences, Moscow, Russian Federation, 2009, pp. 205−224.
[6] M. Sliphorst, B. Knapp, S. Groening, M. Oschwald, Combustion instability-coupling mechanisms between liquid oxygen/methane spray flames and acoustics, J. Propul. Power 28 (2012) 1339−1349.
[7] J. Hardi, M. Oschwald, B. Dally, Flame response to acoustic excitation in a rectangular rocket combustor with LOx/H_2 propellants, CEAS Space Journal 2 (2011) 41−49.
[8] Y. Méry, L. Hakim, P. Scouflaire, L. Vingert, S. Ducruix, S. Candel, Experimental investigation of cryogenic flame dynamics under transverse acoustic modulations, Compt. Rendus Mec. 341 (2013) 100−109.
[9] J.S. Hardi, S.K. Beinke, M. Oschwald, B.B. Dally, Coupling of cryogenic oxygen-hydrogen flames to longitudinal and transverse acoustic instabilities, J. Propul. Power 30 (2014) 991−1004.
[10] J.S. Hardi, H.C.G. Martinez, M. Oschwald, B.B. Dally, LOx jet atomization under transverse acoustic oscillations, J. Propul. Power 30 (2014) 337−349.
[11] L. Hakim, A. Ruiz, T. Schmitt, M. Boileau, G. Staffelbach, S. Ducruix, B. Cuenot, S. Candel, Large eddy simulations of multiple transcritical coaxial flames submitted to a high-frequency transverse acoustic modulation, Proc. Combust. Inst. 35 (2015) 1461−1468.
[12] L. Hakim, T. Schmitt, S. Ducruix, S. Candel, Dynamics of a transcritical coaxial flame under a high-frequency transverse acoustic forcing: influence of the modulation frequency on the flame response, Combust. Flame 162 (10) (2015) 3482−3502.
[13] M. Gonzalez-Flesca, T. Schmitt, S. Ducruix, S. Candel, Large eddy simulations of a transcritical round jet submitted to transverse acoustic modulation, Phys. Fluids 28 (5) (2016) 055106.
[14] J.S. Hardi, Experimental investigation of high frequency combustion instability in cryogenic oxygen-hydrogen rocket engines, PhD Thesis, The University of Adelaide, Adelaide, Australia, 2012.
[15] C. Rey, S. Ducruix, F. Richecoeur, P. Scouflaire, S. Candel, High frequency combustion instabilities associated with collective interactions in liquid propulsion, in: 40th AIAA/ASME/SAE/ASEE Joint Propulsion Conference, Fort Lauderdale, Florida, 2004.
[16] A. Hashimoto, K. Murakami, T. Aoyama, Toward the fastest unstructured CFD Code "FaSTAR", in: 50th AIAA Aerospace Sciences Meeting Including the New Horizons Forum and Aerospace Exposition, Nashville, Tennessee, 2012.
[17] F. Nicoud, F. Ducros, Subgrid-scale stress modelling based on the square of the velocity gradient tensor, Flow, Turbul. Combust. 62 (1999) 183−200.
[18] K. Kitamura, E. Shima, Improvements of simple low-dissipation AUSM against shock instabilities in consideration of interfacial speed of sound, in: 5th European Conference on Computational Fluid Dynamics, 2010, pp. 14−17.
[19] T.C. Horng, M. Ajlan, L.L. Lee, K.E. Starling, M. Ajlan, Generalized multiparameter correlation for nonpolar and polar fluid transport properties, Ind. Eng. Chem. Res. 27 (1988) 671−679.
[20] R.C. Reid, B.E. Poling, J.M. Prausnitz, The Properties of Gases and Liquids, fifth ed., New York, McGraw-Hill, 2001.
[21] G. Ribert, N. Zong, V. Yang, L. Pons, N. Darabiha, S. Candel, Counterflow diffusion flames of general fluids: oxygen/hydrogen mixtures, Combust. Flame 154 (3) (2008) 319−330.
[22] J. Li, Z.W. Zhao, A. Kazakov, F.L. Dryer, An updated comprehensive kinetic model of hydrogen combustion, Int. J. Chem. Kinet. 36 (2004) 566−575.
[23] R.W. Bilger, The structure of turbulent nonpremixed flames, Proc. Combust. Inst. 22 (1988) 475−488.
[24] S.K. Beinke, D. Banuti, J.S. Hardi, M. Oschwald, B.B. Dally, Modelling of a coaxial LOx/GH_2 injection element under high frequency acoustic disturbances, in: 6th European Conference for Aerospace Sciences (EUCASS), Krakow, Poland, 2015.
[25] S.K. Beinke, Analysis of flame response to acoustic forcing in a rocket combustor, PhD Thesis, University of Adelaide, Australia, 2017, http://elib.dlr.de/116739/.
[26] S.C.L. Webster, Analysis of pressure dynamics, forced excitation and damping in a high pressure LOX/H_2 combustor, PhD Thesis, RWTH Aachen, 2016.
[27] S.C.L. Webster, J.S. Hardi, M. Oschwald, One-dimensional model describing eigenmode frequency shift during transverse excitation, in: 6th European Conference for Aerospace Sciences, Torus Press and EDP Sciences, Moscow, Russian Federation, 2017.
[28] S. Gordon, B. McBride, Computer program for calculation of complex chemical equilibrium compositions and applications, NASA Ref. Publ. 1311, 1996.